mathematics

MDPI

Article

Visual Servo Tracking Control and Scene Depth Identification of Mobile Robots with Velocity Saturation Constraints

Qiaomei Zhang *, Baoquan Li and Fuyun Sun

Tianjin Key Laboratory of Intelligent Control of Electrical Equipment, School of Control Science and Engineering, Tiangong University, Tianjin 300387, China; libq@tiangong.edu.cn (B.L.); sunfuyun0411@163.com (F.S.)

* Correspondence: 2231251136@tiangong.edu.cn; Tel.: +86-1820-632-6006

Abstract: Velocity saturation constraints are a significant issue for wheeled mobile robots (WMRs) when designing kinematics-based control laws. To handle the problem of velocity saturation constraints, a novel monocular visual servoing controller is developed for WMRs to solve tracking problems and enable unknown depth estimation. By analyzing the kinematic model of the robot system and employing the homography decomposition technique, measurable signals are obtained to develop a visual tracking error model for non-holonomic mobile robots. To ensure that the velocity commands are consistently constrained within the allowed limits, a saturation function is employed in the designed visual servoing control law. Furthermore, an adaptive updating law is designed to estimate the unknown depth information. The boundedness of the velocity commands is analyzed to evaluate the saturation performance of the developed visual servoing controller. With the aid of Lyapunov techniques and Barbalat's lemma, the stability of this scheme is demonstrated. The simulation and experiment verify the performance of the proposed method.

Keywords: visual servo tracking; velocity saturation; wheeled mobile robots; Lyapunov methods; depth estimation

MSC: 93D05



Academic Editors: Junyong Zhai, Tongxing Li and Valeri Makarov

Received: 27 January 2025
Revised: 9 February 2025
Accepted: 24 February 2025
Published: 27 February 2025

Citation: Zhang, Q.; Li, B.; Sun, F. Visual Servo Tracking Control and Scene Depth Identification of Mobile Robots with Velocity Saturation Constraints. *Mathematics* **2025**, *13*, 790. https://doi.org/10.3390/math13050790

Copyright: © 2025 by the authors. Licensee MDPI, Basel, Switzerland. This article is an open access article distributed under the terms and conditions of the Creative Commons Attribution (CC BY) license (https://creativecommons.org/licenses/by/4.0/).

1. Introduction

Mobile robots are playing an increasingly significant role in various fields, such as smart homes [1], medical services [2], aerospace [3], field exploration [4], and agriculture [5]. In these applications, a camera serves as a robot sensor that provides visual information as feedback to support real-time motion control, commonly referred to as visual servoing [6,7]. In recent decades, visual servoing has become a prominent research topic within the field of robotics. Specifically, traditional visual servoing tasks are generally classified into two main categories: regulation control [8] and tracking control [9–11]. In these tasks, visual information is utilized to direct the robot toward a target position or to track a desired trajectory.

For mobile robot systems, their cognitive abilities, responsiveness, and sensory perception are greatly improved when combined with vision sensors [12]. During vision control, a robot can continuously acquire visual feedback to guide the system toward the desired target position [13], and this is extensively utilized in robot control applications, such as robotic grasping systems [14], surgical robots [15], self-driving cars [16], and lower limb.

Rehabilitation exoskeleton robot [17]. Although GPS-based localization [18] can be used for visual data acquisition, its accuracy and reliability are often inferior to those of

camera-based systems, especially in indoor or complex environments. There are three primary frameworks applied in the current research on current visual servoing: image-based visual servoing [19,20], position-based visual servoing [21,22], and hybrid visual servoing (2.5-DVS) based on homography [23].

Visual servoing represents a rapidly evolving research domain within robotics, and it consists of various methods used to improve robots' performance, making them more intelligent and more environmentally adaptable. However, the lack of scene depth information owing to the perspective projection model of the vision sensors remains a major challenge in visual servoing control, and the estimation of depth information is challenging. In addition, significant problems in the visual tracking task arise from both the nonholonomic constraint and the velocity saturation constraints, especially due to the physical constraints of robots [24]. In practical tasks associated with visual tracking, the attainable velocity of the robot is limited due to upper bounds because the torque output capacity of the robot motor is inherently constrained. When pursuing a fast response, this may lead to the controller generating velocity commands beyond the actuator's capabilities, which affects the control effect and degrades the system's performance; it may even lead to instability [25,26]. Therefore, within the trajectory tracking task in visual control, it remains challenging to ensure that the velocity satisfies the bound constraint despite the unknown depth. Accurate control in complex environments often relies on effectively capturing spatiotemporal dependencies, as seen in thermal error compensation for machining systems [27]. Drawing on these concepts, this study focuses on adaptive visual control for mobile robots, aiming to enhance their trajectory tracking and environmental perception by leveraging visual information in real-time. The main problems studied in this work are trajectory tracking and depth estimation for a wheeled robot, taking into full consideration the velocity saturation constraints by leveraging visual information in real-time.

Regarding velocity saturation, several existing studies have yielded insightful results. In [28], Wang et al. studied the hand–eye visual servo problem for mobile robots with saturated velocity inputs, applying a type of continuously bounded functions to the design of visual servo control. In [29], the authors introduced a framework for stabilization and tracking while considering velocity saturation constraints for wheeled mobile robots, where the saturation function was used to guarantee that there was an upper limit to the velocity command. In [30], a virtual velocity-level controller utilizing a first-order filter was designed. An acceleration-level controller was also designed to achieve the finite-time tracking of the virtual velocity, which could guarantee saturation constraints on the velocity and acceleration. In addition, the authors of [31] proposed a deep reinforcement learning algorithm with adaptive control. The introduction of a guide attention method and a novel velocity-constrained loss function significantly improved obstacle avoidance and velocity control.

To overcome the non-holonomic constraint, various approaches have been proposed, such as adaptive controllers [32]. Adaptive visual servoing technology has become a crucial technique in robotics, enabling the precise control of robotic systems. Unlike traditional visual servoing methods, adaptive visual servoing integrates real-time visual feedback with adaptive control algorithms, significantly enhancing the accuracy and robustness of robotic systems. In [33], this study reviews the applications of reinforcement learning and adaptive control in improving intelligent robots' path planning and navigation. A novel method based on these techniques is proposed and experimentally validated, showing significant performance improvements. This research provides theoretical and methodological support to enhance robots' efficiency in complex environments. In [34], a data-driven time–frequency analysis (TFA) technique called CTNet was proposed. By integrating a fully convolutional autoencoder network with an adaptive attention mechanism

(CBAM), CTNet could effectively identify complex time–frequency patterns and improve the fault detection accuracy. This approach demonstrates the potential of combining data-driven models for parameter identification with adaptive control algorithms to enhance systems' reliability in dynamic environments.

In addition, the absence of depth parameters remains an inherent challenge, and there has been some research in this area. With an abundance of recorded data, an adaptive trajectory tracking controller was developed, which was dependent on homography using the concept of concurrent learning techniques. This facilitated the task of estimating the tasks of estimating the scene depth while improving the trajectory performance and ensuring exponential convergence [35]. In [36], to solve the problem of the visual servo regulation task, the homography matrix decomposition and concurrent learning technique were applied to the design of an adaptive updating law. Utilizing both recorded and real-time data, the unknown depth could be estimated simultaneously. In [37], applying the PE condition, an augmented updating law was designed that depended on a reduced-order observer to compensate for unknown depth information while simultaneously estimating the inverse depth. In [38], a resilient adaptive tracking control scheme was proposed for uncalibrated visual servoing systems with unknown actuator failures, effectively handling the time-varying depth and ensuring the asymptotic convergence of tracking errors through adaptive algorithms and dynamic decoupling; this is validated using simulation results. In [39], the authors proposed an adaptive visual servoing method using I&I fuzzy logic for omnidirectional mobile robots, ensuring robustness against dynamic uncertainties and improving the system's stability.

Inspired by the work in [40], this study introduces an adaptive visual servo strategy for mobile robots to achieve the task of trajectory tracking and depth estimation under velocity saturation constraints. Firstly, the robot system is described in detail, and the relationship between the coordinate systems is presented. After an analysis of the kinematic model and employing the homography decomposition technique, the visual tracking error model is developed using measurable signals. To ensure that the generated velocity commands do not exceed the specified saturation limits, a saturation function is incorporated into the design of the vision-based control law. In addition, as the adaptive updating law satisfies the PE condition, it enables the identification of the unknown depth information. Subsequently, to clearly illustrate the saturation performance of the designed visual servoing controller, the constraints on the velocity commands are assessed, and appropriate guidelines for parameter selection are provided accordingly. Meanwhile, after employing Lyapunov techniques and Barbara's theorem, a rigorous stability analysis is performed. Both the simulation and experiment verify the effectiveness of the proposed scheme. The primary contributions of this work are the following:

(1) An adaptive visual servo trajectory tracking controller with the velocity saturation constraint is proposed for wheeled mobile robots, which is successful despite the unknown depth.
(2) The unknown depth is not only adaptively updated online but can also be simultaneously identified during the visual servoing process.
(3) Compared with the existing controller in [40], the proposed controller can theoretically achieve asymptotic stability in the presence of both saturation constraints and an unknown depth, and both simulation and experiment confirm the effectiveness of the system.

In Section 2, the vision-based mobile robot system model and the kinematic model are described. Section 3 describes the design process of the tracking controller, and a rigorous demonstration of the stability of the robotic system is provided. Sections 4 and 5 describe the simulation and experiment. Finally, the conclusion is given in Section 6.

2. Related Work

2.1. Description of Robot System

Figure 1 shows the relative positional relations of the coordinate system of the wheeled mobile robot, where the camera frame is assumed to coincide with the robot's frame. The global reference pose is represented by $\mathcal{F}^*$, while the current coordinate frame associated with the camera is denoted by $\mathcal{F}^c$, where x^C is defined to be oriented towards the robot, being directly in front. The x^C-axis is directed towards the front of the robot, aligning with its heading, and the y^c-axis runs parallel to the wheel axis. The z^c-axis is fixed at the center point of the wheel axis and is perpendicular to the plane of motion. We denote by $\mathcal{F}^d$ the desired pose on the desired trajectory of a given robot. In addition, the angles of rotation of $\mathcal{F}^c$ and $\mathcal{F}^d$ are expressed as $\theta(t) \in [-\pi, \pi]$ and $\theta^d(t) \in [-\pi, \pi]$, respectively.

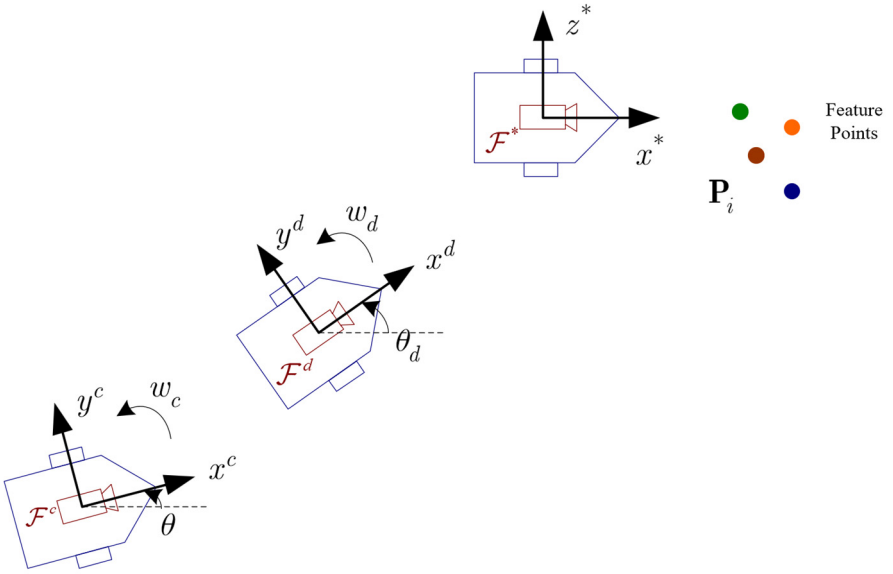


Figure 1. Relationships in the coordinate system.

It is generally assumed that a minimum of four static feature points P_i, which are both coplanar and non-collinear, are situated on the plane π. Additionally, $d^* \in \mathbb{R}^+$ represents an unknown constant that is used to indicate the distance from the origin of the reference frame $\mathcal{F}^*$ to the plane π. During the visual servoing process, $\mathcal{F}^*$ remains relatively stationary concerning the plane π.

In Figure 2, an overall graphical depiction of the proposed method is illustrated. The closed-loop control system comprises an adaptive updating law designed to estimate the unknown scene depth and a velocity saturation controller. Moreover, the adaptive updating law enables depth estimation during the tracking process.

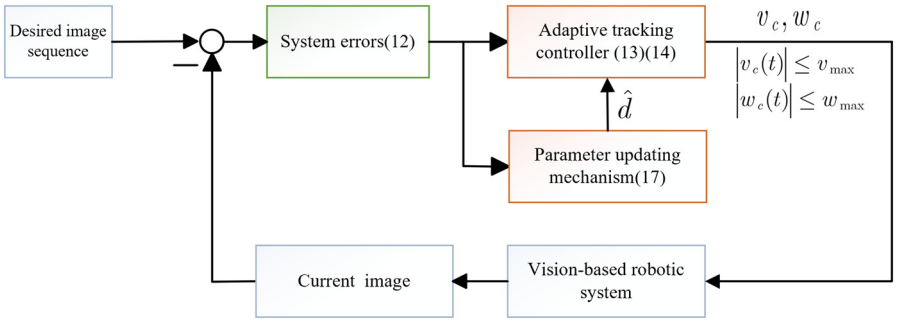


Figure 2. Block diagram of the mobile robot system.

2.2. Kinematic Model

The static target plane π consists of W coplanar feature points p_i (i = 1, 2, …, W). The Euclidean coordinates of p_i in $\mathcal{F}^c$, $\mathcal{F}^d$, and $\mathcal{F}^*$ are represented as P_i, ${P_i}^d$, and ${P^*}_i$, respectively, written as follows:

$$\begin{cases} P_i = [X_i, Y_i, Z_i]^T \\ {P^d}_i = \left[{X^d}_i, {Y^d}_i, {Z^d}_i\right]^T \\ {P^*}_i = [{X^*}_i, {Y^*}_i, {Z^*}_i]^T \end{cases}. \tag{1}$$

The rotation matrix that transforms the coordinate system from $\mathcal{F}^*$ to $\mathcal{F}^c$ is represented as ${}^c_*R(t) \in SO(3)$, while the corresponding translation vector is represented by $x_f(t) \in R^3$. Likewise, the rotation matrix and the translation vector from $\mathcal{F}^*$ to $\mathcal{F}^d$ are expressed as ${}^d_*R(t) \in SO(3)$ and $x_{fd}(t) \in R^3$, respectively. Since the movement of the wheeled mobile robot is constrained in the xy-plane, the position components $x_f(t)$ and $x_{fd}(t)$ are denoted as follows:

$$\begin{aligned} x_f(t) &\triangleq \begin{bmatrix} x_{f1} & x_{f2} & 0 \end{bmatrix}^T \\ x_{f\mathrm{d}}(t) &\triangleq \begin{bmatrix} x_{fd1} & x_{fd2} & 0 \end{bmatrix}^T. \end{aligned} \tag{2}$$

Based on the principle of frame transformation, relationships among $P_i(t)$, ${P^{\mathrm{d}}}_i(t)$, and ${P^*}_i(t)$ are as follows:

$$\begin{cases} P_i = x_f + {}^c_*R{P^*}_i \\ {P^{\mathrm{d}}}_i = x_{fd} + {}^d_*R{P^*}_i \end{cases}. \tag{3}$$

In (3), we define ${}^c_*R$ and ${}^d_*R$ as follows:

$${}^c_*R \triangleq \begin{bmatrix} \cos\theta_c & -\sin\theta_c & 0 \\ \sin\theta_c & \cos\theta_c & 0 \\ 0 & 0 & 1 \end{bmatrix}, {}^d_*R \triangleq \begin{bmatrix} \cos\theta_d & -\sin\theta_d & 0 \\ \sin\theta_d & \cos\theta_d & 0 \\ 0 & 0 & 1 \end{bmatrix}, \tag{4}$$

where θ_c is the angle of rotation of frame $\mathcal{F}^c$ relative to $\mathcal{F}^*$, while θ_d denotes the angle of rotation of $\mathcal{F}^d$ relative to $\mathcal{F}^*$. The following is clear from Figure 1 and Equation (4):

$$\dot{\theta}_c = -w_c, \dot{\theta}_d = -w_{cd}, \tag{5}$$

where w_{cd} represents the desired angular velocity of the WMRs, expressed in the frame $\mathcal{F}^d$.

2.3. Euclidean Reconstruction

In the desired, current, and reference images, the corresponding feature points are denoted as ${p^{\mathrm{d}}}_i(t)$, $p_i(t)$, and ${p^*}_i(t)$, respectively. Based on the principles of projective geometry, the relationships between the Euclidean coordinates of the target points and the image data can be formulated as follows:

$$p_i = K\frac{P_i}{x_i}, \ {p^d}_i = K\frac{{P_i}^d}{{x^d}_i}, \ p^*i = K\frac{{P_i}^*}{{x^*}_i}, \tag{6}$$

where $K \in \mathbb{R}^{3\times3}$ is the camera's intrinsic matrix, which is a constant, known, and invertible parameter that can be calibrated offline.

Furthermore, the unit normal vector of the feature plane π is denoted as $n^* = [n_x^* \quad n_y^* \quad n_z^*]^T \in \mathbb{R}^3$. The distance from $\mathcal{F}^*$ to π along n^* representing the scene depth $d^* \in R$, is expressed as follows:

$$d^* = {n^*}^T P_i^*, \tag{7}$$

where the constant d^* represents the scene depth information.

Based on (3), (6), and (7), the correlations among the image feature points can be derived as follows:

$$\begin{cases} p_i = \underbrace{\frac{x^*{}_i}{x_i}}_{\alpha_i} \underbrace{K({}^c_*R + x_h n^{*T})K^{-1}p^*{}_i}_{G} \\ p_i^d = \underbrace{\frac{x^*{}_i}{x^d{}_i}}_{\alpha_i^d} \underbrace{K\left({}^d_*R + x_{hd} n^{*T}\right)K^{-1}}_{G_{\mathrm{d}}} p^*{}_i \end{cases}, \tag{8}$$

where $\alpha_i \in \mathbb{R}$ and $\alpha_{\mathrm{i}}^d \in \mathbb{R}$ denote the depth ratios, while $G(t)$ and $G_d(t)$ are projection Euclidean homographies. x_h and x_{hd} denote the scaled translation vectors, written as follows:

$$\begin{cases} x_h \triangleq \begin{bmatrix} x_{h1} & x_{h2} & 0 \end{bmatrix}^T = \frac{x_f}{d^*} \\ x_{hd} \triangleq \begin{bmatrix} x_{hd1} & x_{hd2} & 0 \end{bmatrix}^T = \frac{x_{fd}}{d^*} \end{cases}. \tag{9}$$

3. Development of Control Algorithm

3.1. Error System

From (8), Euclidean reconstruction technologies can be applied to achieve the decomposition of $G(t)$ and $G_{\mathrm{d}}(t)$, and it is clear from the decomposition results that ${}^c_*R$, ${}^d_*R$, x_h, x_{hd}, θ_c, and θ_d are measurable signals.

Furthermore, according to a previous study, the tracking errors for translation and rotation, represented as $e(t) \triangleq [e_1\ e_2\ e_3]^T$, are formulated as follows:

$$\begin{cases} e_1 = x_{h1} - x_{hd1} \\ e_2 = x_{h2} - x_{hd2} \\ e_3 = \theta_c - \theta_{\mathrm{d}} \end{cases}. \tag{10}$$

To support the further developments, an auxiliary variable $\bar{e}_2 \in R$ is introduced, written as follows:

$$\bar{e}_2 = e_2 - x_{hd1} e_3. \tag{11}$$

After further derivation, the dynamics of the open-loop error can be represented as follows:

$$\begin{cases} d^* \dot{e}_1 = -v_c + d^*(x_{h2} w_c - \dot{x}_{hd1}) \\ \dot{\bar{e}}_2 = -(e_1 w_c + \dot{x}_{hd1} e_3). \\ \dot{e}_3 = -(w_c + \dot{\theta}_d) \end{cases} \tag{12}$$

3.2. Velocity Saturation Controller Design

To successfully execute the trajectory tracking task, the control inputs for the mobile robot are formulated as follows:

$$v_c = k_1 \tanh(e_1) - d^* \bar{e}_2 w_c + \hat{d}^*(x_{h2} w_c - \dot{x}_{hd1}), \tag{13}$$

$$w_c = k_2 \tanh(e_3) - \dot{\theta}_d - \frac{k_3 d^* \bar{e}_2 \dot{x}_{hd1}}{1 + {e_1}^2 + {\bar{e}_2}^2}, \tag{14}$$

where the constants k_1, k_2, and k_3 denote positive control gains. By incorporating the motion control signals from Equations (13) and (14) into Equation (12), the following closed-loop error system can be obtained :

$$\begin{cases} d^*\dot{e}_1 = -k_1\tanh(e_1) + d^*\bar{e}_2 w_c + \widetilde{d}^*(x_{h2}w_c - \dot{x}_{hd1}) \\ \dot{\bar{e}}_2 = -(e_1 w_c + \dot{x}_{hd1}e_3) \\ \dot{e}_3 = -k_2\tanh(e_3) + \frac{k_3 d^*\bar{e}_2\dot{x}_{hd1}}{1+{e_1}^2+{\bar{e}_2}^2} \end{cases}. \tag{15}$$

$\widetilde{d}^* \in \mathbb{R}^+$ denotes the scene depth estimate error, calculated as follows:

$$\widetilde{d}^* = d^* - \hat{d}^*, \tag{16}$$

where $\hat{d}^*(t)$ represents the estimated scene depth. As $\widetilde{d}^*(t)$ approaches zero, the scene depth information is accurately estimated.

For the depth estimation problem, the adaptive update law is designed as follows:

$$\dot{\hat{d}}^* = \Gamma \mathrm{Pro}j_{\hat{d}}\left(\frac{k_3 e_1(x_{h2}w_c - \dot{x}_{hd1})}{1+{e_1}^2+{\bar{e}_2}^2}\right), \tag{17}$$

where $\Gamma \in R^+$ represents the positive updating gain. Then, the corresponding projection function $\mathrm{Pro}j_{\hat{d}}(*)$ is denoted as shown below:

$$\mathrm{Pro}j_{\hat{d}}(*)\begin{cases} 0, & for(\hat{d}^* = {d^*}_{\min}\ and * < 0)or \\ & (\hat{d}^* = {d^*}_{\max}\ and * > 0) \\ *, & else \end{cases}, \tag{18}$$

where ${d^*}_{\max} \in R^+$ and ${d^*}_{\min} \in R^+$ represent the positive upper and lower bound of the unknown depth, respectively.

Combining (17) and (18), two conclusions can be further obtained, written as follows:

$$\hat{d}^* \in \Phi_d = \{d^* : 0 < {d^*}_{\min} \le d^* \le {d^*}_{\max}\}, \tag{19}$$

$$\widetilde{d}^*\mathrm{Pro}j_{\hat{d}}(*) \ge \widetilde{d}^*\left(\frac{k_3 e_1(x_{h2}w_c - \dot{x}_{hd1})}{1+{e_1}^2+{\bar{e}_2}^2}\right). \tag{20}$$

Thus, it can be concluded that the estimated value $\hat{d}^*(t)$ remains bound within $[{d^*}_{\min}, {d^*}_{\max}]$.

3.3. Stability Analysis

Theorem 1. *Employing the controllers given in Equations (13) and (14) along with the parameter update law given in Equation (17), the system can ensure that the errors converge to zero in the sense that* $\lim_{t\to\infty} e_1, e_2, e_3 = 0$. *In addition, the update laws given in (17) ensure that the unknown depth information can be estimated at the same time.*

Proof. According to the given model, the Lyapunov candidate function $V(t)$ is expressed as follows:

$$V = d^*\frac{\mathrm{k}_3}{2}\log(1+{e_1}^2+{\bar{e}_2}^2) + \frac{1}{2}{e_3}^2 + \frac{1}{2}\Gamma^{-1}\widetilde{d}^{*2}. \tag{21}$$

Since $d*$ is positive according to Equation (16), it follows that $V(t) \ge 0$. After computing the temporal derivative of Equation (21) and applying the control law (13), (14), and closed-loop system (15), the following equation is obtained:

$$\begin{aligned} \dot{V}(t) = {} & \frac{-k_1 k_3 e_1\tanh(e_1)}{1+{e_1}^2+{\bar{e}_2}^2} - k_2 e_3\tanh(e_3) \\ & + \widetilde{d}^*\frac{k_3 e_1(x_{h2}w_c - \dot{x}_{hd1})}{1+{e_1}^2+{\bar{e}_2}^2} + \Gamma^{-1}\widetilde{d}^*\dot{\widetilde{d}}^*. \end{aligned} \tag{22}$$

Then, substituting the depth estimation error (16) and the adaptive updating law (17) into (22), the following is obtained:

$$\begin{aligned}\dot{V}(t) &= \frac{-k_1 k_3 e_1 \tanh(e_1)}{1+{e_1}^2+{\bar{e}_2}^2} - k_2 e_3 \tanh(e_3) \\ &+\widetilde{d}^* \frac{k_3 e_1 (x_{h2} w_c - \dot{x}_{hd1})}{1+{e_1}^2+{\bar{e}_2}^2} - \widetilde{d}^* \mathrm{Pro}j_{\hat{d}}[\frac{k_3 e_1 (x_{h2} w_c - \dot{x}_{hd1})}{1+{e_1}^2+{\bar{e}_2}^2}].\end{aligned} \tag{23}$$

Based on the inequality in (20), the following is obtained:

$$\widetilde{d}^* \frac{k_3 e_1 (x_{h2} w_c - \dot{x}_{hd1})}{1+{e_1}^2+{\bar{e}_2}^2} - \widetilde{d}^* \mathrm{Pro}j_{\hat{d}}[\frac{k_3 e_1 (x_{h2} w_c - \dot{x}_{hd1})}{1+{e_1}^2+{\bar{e}_2}^2}] \leq 0. \tag{24}$$

Thus, it follows that $\dot{V}(t) \leq 0$. Moreover, since $V(t) \geq 0, \dot{V}(t) \leq 0$, we know the following:

$$e_1, \bar{e}_2, e_3, \widetilde{d}^* \in \mathcal{L}_\infty, \tag{25}$$

and, from Equation (16), it follows that $\hat{d}^* \in \mathcal{L}_\infty$. For the desired trajectory, the boundedness of $x_{hd1}(t)$, $\dot{x}_{hd1}(t)$, $x_{hd2}(t)$, $\theta_d(t)$, and $\dot{\theta}_d(t)$ is ensured. Given the condition that $\bar{e}_2, e_3 \in \mathcal{L}_\infty$, the expressions in (10), (11), and (14) can be utilized to demonstrate that $e_2(t), x_{h1}(t), x_{h2}(t), \theta_c(t), w_c(t) \in \mathcal{L}_\infty$. Furthermore, from Equations (12), (13) and (17), we know the following:

$$v_c, \dot{e}_1(t), \dot{\bar{e}}_2(t), \dot{e}_3(t), \dot{\hat{d}}^* \in \mathcal{L}_\infty. \tag{26}$$

Therefore, $e_1(t), e_2(t), e_3(t), \widetilde{d}^*$ and $\hat{d}^*$ are uniformly continuous.

From $\dot{V}(t) \leq 0$ and (22), because $-\dot{V}(t) = \frac{k_1 k_3 e_1 \tanh(e_1)}{1+{e_1}^2+{\bar{e}_2}^2} + k_2 e_3 \tanh(e_3) - (\widetilde{d}^*(x_{h2} w_c - \dot{x}_{hd1}) \frac{k_3 e_1}{1+{e_1}^2+{\bar{e}_2}^2} - \widetilde{d}^* \mathrm{Pro}j_{\hat{d}}[\frac{k_3 e_1 (x_{h2} w_c - \dot{x}_{hd1})}{1+{e_1}^2+{\bar{e}_2}^2}])$, and $-(\widetilde{d}^* \frac{k_3 e_1}{1+{e_1}^2+{\bar{e}_2}^2}(x_{h2} w_c - \dot{x}_{hd1}) - \widetilde{d}^* \mathrm{Pro}j_{\hat{d}}[\frac{k_3 e_1 (x_{h2} w_c - \dot{x}_{hd1})}{1+{e_1}^2+{\bar{e}_2}^2}]) \geq 0$, we obtain the following

$$\frac{k_1 k_3 e_1 \tanh(e_1)}{1+{e_1}^2+{\bar{e}_2}^2} + k_2 e_3 \tanh(e_3) \leq -\dot{V} \tag{27}$$

and, by performing integration on both sides of the inequality, we obtain the following:

$$\int_0^\infty \left(\frac{k_1 k_3 e_1 \tanh(e_1)}{1+{e_1}^2+{\bar{e}_2}^2} + k_2 e_3 \tanh(e_3) \right) dt \leq -\int_0^\infty \dot{V} dt. \tag{28}$$

Considering the right-hand expression of the given equation, since $V(t) \geq 0$ and $\dot{V}(t) \leq 0$, $V(t)$ is non-increasing with a lower bound. Hence, the following is known:

$$-\int_0^\infty \dot{V} dt = V(0) - V(\infty) \leq V(0). \tag{29}$$

Therefore, the integral $\int_0^\infty \left(\frac{k_1 k_3 e_1 \tanh(e_1)}{1+{e_1}^2+{\bar{e}_2}^2} + k_2 e_3 \tanh(e_3) \right) dt$ is finite. Moreover, since integral components $e_1(t), \bar{e}_2(t), e_3(t)$ are uniformly continuous, the system remains uniformly continuous. According to Barbalat's lemma, the following conclusion can be drawn:

$$\lim_{t \to \infty} \frac{k_1 k_3 e_1 \tanh(e_1)}{1+{e_1}^2+{\bar{e}_2}^2} + k_2 e_3 \tanh(e_3) = 0 \tag{30}$$

where k_1, k_2, and k_3 are positive constants, and $e_1 \tanh(e_1) \geq 0$ and $e_3 \tanh(e_3) \geq 0$. Therefore, (30) can be rewritten as follows:

$$\lim_{t \to \infty} e_1 \tanh(e_1) = 0, \lim_{t \to \infty} e_3 \tanh(e_3) = 0 \tag{31}$$

If and only if $e_1, e_3 = 0$, $e_1\tanh(e_1) \geq 0$, and $e_3\tanh(e_3) \geq 0$. The following can therefore be proven:

$$\lim_{t\to\infty} e_1 = 0, \lim_{t\to\infty} e_3 = 0. \tag{32}$$

According to the error system (15), we obtain the following:

$$\dot{e}_3 = -(w_c + \dot{\theta}_d) = -k_2\tanh(e_3) + \frac{k_3 d^* \bar{e}_2 \dot{x}_{hd1}}{1 + {e_1}^2 + {\bar{e}_2}^2}. \tag{33}$$

Let the following be true:

$$g_1(t) = -k_2\tanh(e_3), g_2(t) = \frac{k_3 d^* \bar{e}_2 \dot{x}_{hd1}}{1 + {e_1}^2 + {\bar{e}_2}^2}. \tag{34}$$

Since all components of $g_2(t)$ are uniformly continuous, it follows that $g_2(t)$ itself is uniformly continuous. From (31) and (32), the following can be shown:

$$\lim_{t\to\infty} e_3 = 0, \lim_{t\to\infty} g_1(t) = 0. \tag{35}$$

Thus, based on the principles of the extended Barbalat's lemma, the following conclusions are obtained: $\lim_{t\to\infty} \dot{e}_3(t) = \lim_{t\to\infty} g_1(t) + g_2(t) = 0$, $\lim_{t\to\infty} g_2(t) = 0$. This means the following can be obtained:

$$\lim_{t\to\infty} \frac{k_3 d^* \bar{e}_2 \dot{x}_{hd1}}{1 + {e_1}^2 + {\bar{e}_2}^2} = 0. \tag{36}$$

Since k_3,$d^* \neq 0$, it follows that $\lim_{t\to\infty} \bar{e}_2 = 0$, provided that the condition $\lim_{t\to\infty} \dot{x}_{hd1} \neq 0$ is satisfied. From the definition of $e_2(t)$, (32), and $\lim_{t\to\infty} \bar{e}_2 = 0$, it can be found that $\lim_{t\to\infty} e_2 = 0$. □

3.4. Analysis of Signal Boundedness

Here, the velocities v and w of the mobile robot are used as the inputs and should satisfy the constraints:

$$|v_c(t)| \leq v_{\max}, |w_c(t)| \leq w_{\max}, \forall t \geq 0 \tag{37}$$

where $v_{\max} > sup_{t\geq 0}|v_{rd}(t)|$ and $w_{\max} > sup_{t\geq 0}|w_{rd}(t)|$ are given arbitrary positive constants and denote the maximum values of the saturation constraints, respectively. The goal is to control the velocities of the wheeled mobile robot to track the desired trajectory under saturation constraints.

For $w_c(t)$, $w_{\mathrm{d}} \leq |w_{\mathrm{d}}|_{\max}$, $|\tanh(e_3)| \leq 1$ and $d^* \leq {d^*}_{\max}$; thus, we obtain the following:

$$w_c \leq k_2 + |w_{\mathrm{d}}|_{\max} + \left| \frac{k_3 d^* \bar{e}_2 \dot{x}_{hd1}}{1 + {e_1}^2 + {\bar{e}_2}^2} \right| \tag{38}$$

where

$$\frac{\bar{e}_2}{1 + {e_1}^2 + {\bar{e}_2}^2} \leq 0.5. \tag{39}$$

The upper limit of $|\mathrm{w}_c|$ is determined as follows:

$$w_c \leq k_2 + |w_{\mathrm{d}}|_{\max} + \frac{k_3}{2}|d^*|_{\max}|\dot{x}_{hd1}|_{\max}. \tag{40}$$

For $v_c(t)$, $|\tanh(e_1)| \leq 1$, $w_c \leq |w_c|_{\max}$, $\hat{d}^* \leq d^*{}_{\max}$, $x_{h2} \leq |x_{h2}|_{\max}$, and $\dot{x}_{hd1} \leq |\dot{x}_{hd1}|_{\max}$. From (36), $\bar{e}_2$ tends to 0. Thus, the bound of $|v_c|$ can be derived as follows:

$$v_c \leq k_1 + d^*{}_{\max}\left[|x_{hd2}|_{\max}|w_c|_{\max} - |\dot{x}_{hd1}|_{\max}\right]. \tag{41}$$

Hence, the constraints on the upper-velocity commands can be defined using (40) and (41), i.e., velocity bounds $|v| \leq \lambda_v$ and $|w| \leq \lambda_w$ can be satisfied by appropriately tuning k_1, k_2, and k_3.

4. Simulation Results

The simulation confirms the effectiveness of the proposed method. The homography is acquired by randomly placing four coplanar feature points. For the camera, the intrinsic parameters K are defined as follows:

$$K = \begin{bmatrix} 1003.7 & 0 & 376.9 \\ 0 & 1006.3 & 285.3 \\ 0 & 0 & 1 \end{bmatrix}. \tag{42}$$

The selected values for the control parameters are $k_1 = 0.7$, $k_2 = 0.09$, $k_3 = 0.75$, and $\Gamma = 40$.

Figure 3 shows the motion paths of the wheeled mobile robot, where the red path is the desired path, and the blue path is the current path; the graph demonstrates that the robot can closely follow the desired trajectory, as indicated by the minimal deviation between the red and blue lines throughout the motion. This result indicates that the robot successfully tracks the desired trajectory. Figure 4 illustrates the evolution of the tracking errors over time. The results demonstrate that all three error components converge smoothly to zero, confirming the performance of the proposed control method in achieving accurate trajectory tracking and system stability.

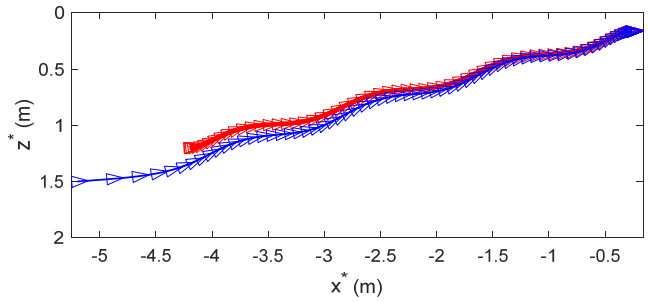


Figure 3. Motion trajectories of the mobile robot.

Figure 5 shows the velocities of the robot, where the desired velocity inputs are represented by the red dotted lines, the yellow dotted lines reflect the virtual velocity saturation limits (λ_v and λ_w), and the blue solid lines correspond to the current velocities. It can be seen that the actual velocity closely matches the desired velocity, and the robot can perform stable velocity tracking within the range of the given velocity saturation constraints. Figure 6 presents image trajectories of feature points during the simulation process, with dashed lines representing the desired feature trajectories and solid lines indicating the actual trajectories achieved by the mobile robot. It is evident that the actual feature trajectories closely follow the desired paths, demonstrating the validity of the proposed control strategy in achieving accurate trajectory tracking. Figure 7 shows the evolution of the estimated depth when using the adaptive updating law. From the figure, it is evident that the estimated depth rapidly converges to the actual value within approximately 10 s and maintains stability thereafter, with minor fluctuations. This demonstrates the validity of the developed adaptive updating law in enabling the accurate estimation of the unknown depth.

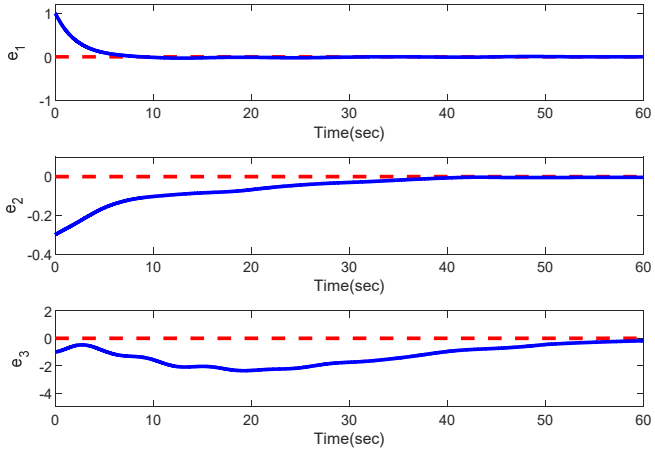


Figure 4. Evolution of the robot errors.

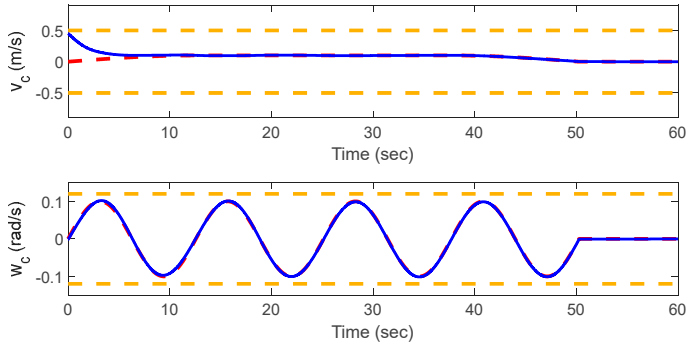


Figure 5. Velocities of the mobile robot. The yellow dotted lines denote the velocity saturation limits.

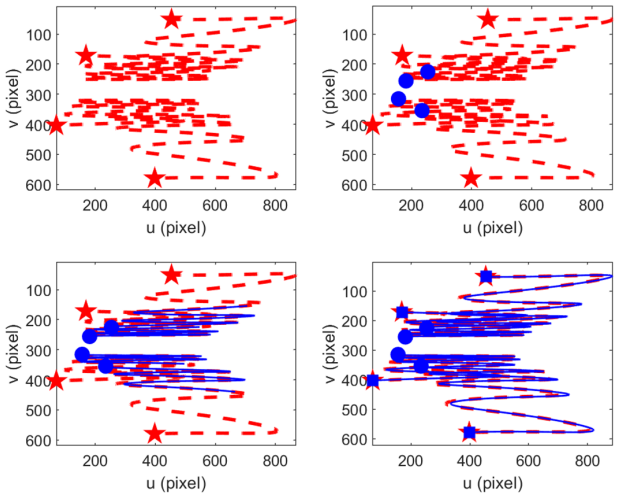


Figure 6. Image paths of feature points.

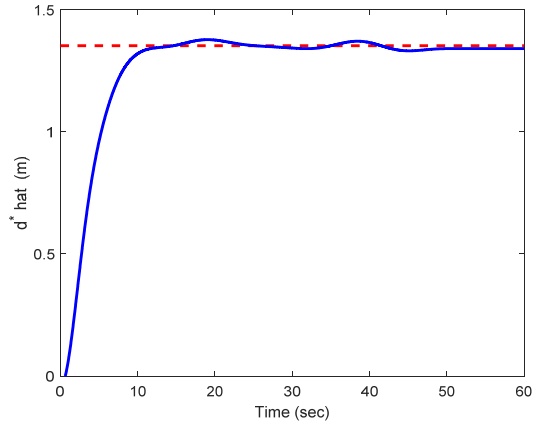


Figure 7. Evolution of $\hat{d}^*$ when using the adaptive updating law (dashed line: true value of d^*).

In addition, this paper tests the robustness of the proposed controller to noise by gradually increasing the intensity of Gaussian noise in the experiments. Specifically, we compare the performance of our controller with that in [13], where a random image noise with a standard deviation of σ = 0.15 pixels is applied to test the robustness of the proposed control law. In our study, we set the noise levels at σ = 0.3 pixels. Furthermore, the trajectory complexity in our experiments is significantly higher than that in [13], which involves simpler trajectories. The simulation results are illustrated in Figures 8–10, sequentially depicting the evolution of robot errors, velocities of the mobile robot, and depth estimation. As can be seen from Figures 8–10, the proposed controller demonstrates excellent stability, even with the increased noise and more complex tracking scenarios. This highlights the effectiveness and robustness of the proposed control strategy in handling more challenging conditions while maintaining high performance.

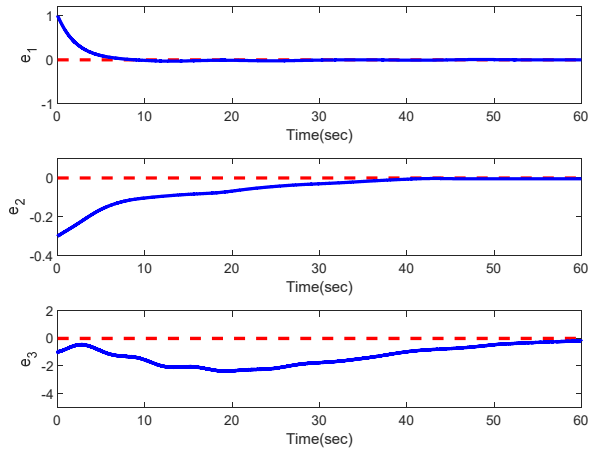


Figure 8. Evolution of the robot errors with noise.

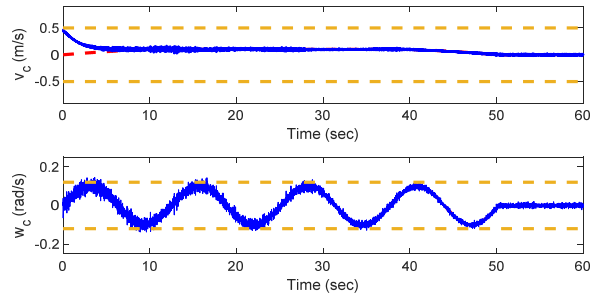


Figure 9. Velocities of the mobile robot with noise. The yellow dotted lines denote the velocity saturation limits.

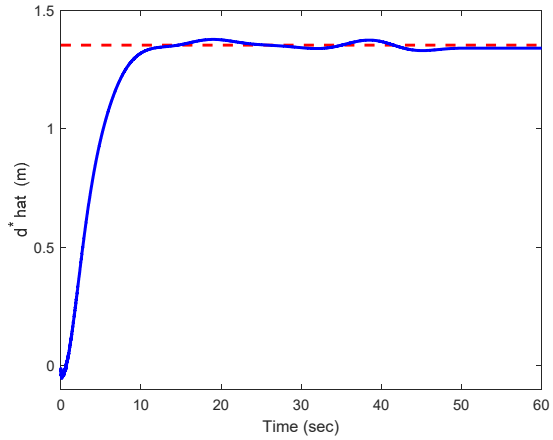


Figure 10. Evolution of $\hat{d}^*$ by the adaptive updating law with noise (dashed line: truth value of d^*).

5. Experimental Verification

In this section, the effectiveness of the proposed control strategy is further verified by drawing on the experimental results. As depicted in Figure 11, the experimental setup utilizes a Pioneer3-AT mobile robot fitted with a DMK23G618 camera. The camera is mounted at the center of the robot to ensure that the coordinate system of the camera corresponds to that of the robot. The experimental platform also includes a laptop computer, which communicates with the camera through a USB 3.0 port and with the mobile robot through an RS-232 serial port. The camera has an image size of 640 × 480 pixels and supports a maximum frame rate of 120 frames per second. The experiments are conducted indoors on a flat floor, where four coplanar artificial corner points are used to enhance the accuracy of robot pose information derived from the homography matrix. These feature points are determined using every shared vertex of adjacent squares. For control algorithm processing, the experiments are implemented in a C++ environment using the OpenCV library within the Visual Studio IDE. The intrinsic parameter is conducted using MATLAB R2020b during the experiment. The results of the offline calibration of the camera's intrinsic parameter matrix are provided as follows:

$$k = \begin{bmatrix} 825.05586 & 0 & 326.82740 \\ 0 & 824.45217 & 228.87652 \\ 0 & 0 & 1 \end{bmatrix}. \tag{43}$$

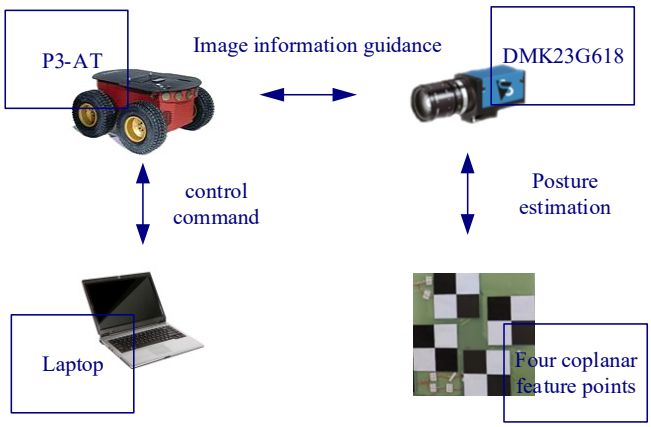




Figure 11. Experimental setup: visual features and mobile robot platform.

Two experimental trials are carried out to demonstrate the effectiveness of the developed strategy. In the first experiment, the visual servoing tracking problem in the presence of an unknown depth is solved using the proposed method. Two different velocity limits are set for comparison, with the purpose of demonstrating that the proposed control strategies are sufficient to complete the required tasks within different saturation constraints. To further assess the proposed strategy, a comparison is conducted with the existing method presented in [40].

To perform an objective comparison between the method proposed in this work and the compared method, two contrast experiments are performed in the same situation. Specifically, the desired trajectory begins from an initial position (-2.01 m, -0.002 m, 1.57°) and then moves in a snake-like motion. λ_{v} and λ_w are set as the upper velocity limits, where $\lambda_{\mathrm{v}1} = 0.10$ m/s, $\lambda_{v2} = 0.08$ m/s, and $\lambda_w = 0.2$ rad/s, respectively. For the proposed strategy, the parameters of the control law and adaptive updating law are assigned values of $k_1 = 0.6$, $k_2 = 0.5$, $k_3 = 0.5$, $\Gamma = 30$, with the initial unknown depth specified as $\hat{d}^*(0) = 0.10$ m. In Figures 12–16, the experimental results are presented in the form of similar data types in a single graph, effectively demonstrating the proposed method's advantages.

Figure 12 provides the desired and current motion trajectories. In Figure 12, the first and second plots correspond to the two different virtual velocity constraints λ_{v} designed using the method proposed in this work, while the third plot corresponds to the method in [40]. In all plots, the desired motion path is depicted by the red solid line, whereas the blue solid line indicates the actual motion path. The figure indicates that the proposed method achieves accurate trajectory tracking under both velocity constraints, as shown in the first and second plots. The blue solid lines closely follow the red dashed lines, showing the performance of the developed control method in ensuring precise path tracking. By contrast, the third plot reveals larger deviations between the desired and actual paths when using the method from [40], highlighting its comparatively lower tracking accuracy under the same experimental conditions. These results confirm the robustness and adaptability of the proposed method in handling different velocity constraints while maintaining superior tracking performance.

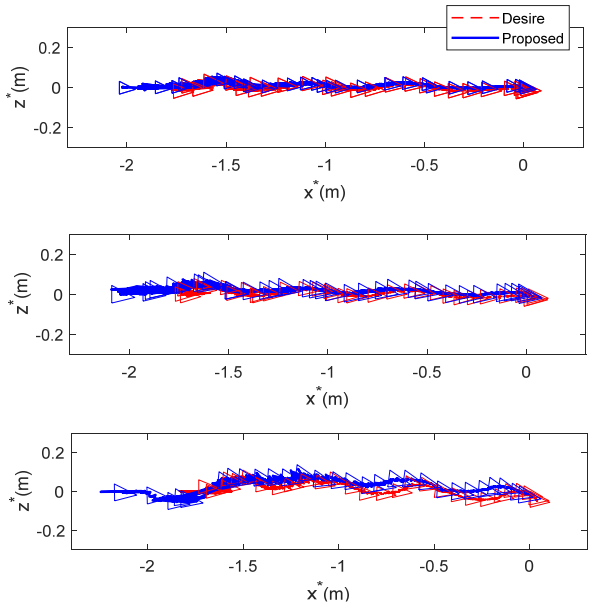


Figure 12. Motion trajectories of the current and desired frames under $\mathcal{F}^*$. The first and second plots correspond to two different velocity constraints set using the control method introduced in this work, while the third plot corresponds to the previous method in [40]. Red solid lines: desired motion trajectories; blue solid lines: current motion trajectories.

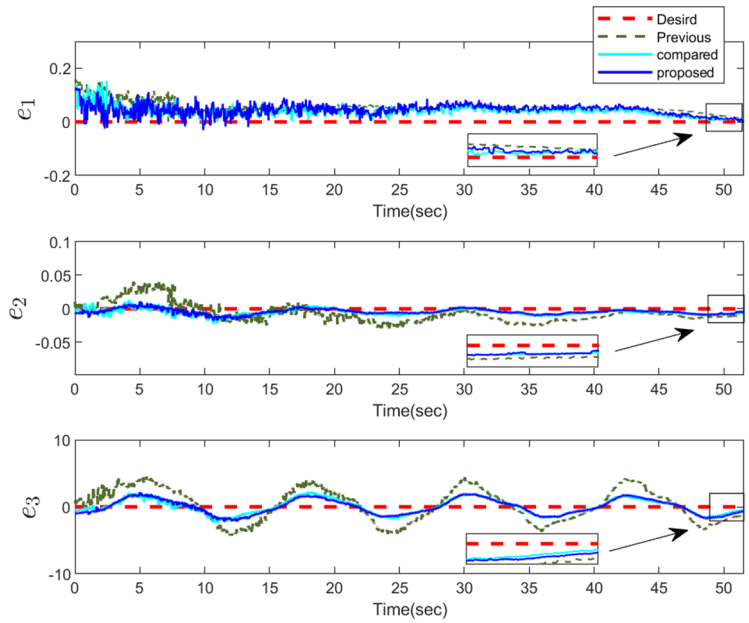


Figure 13. Evolution of trajectory tracking errors. The dark blue and light blue solid lines denote the two different velocity constraints imposed with the control method proposed in this work, respectively, and the green dashed line corresponds to the previous method in [40].

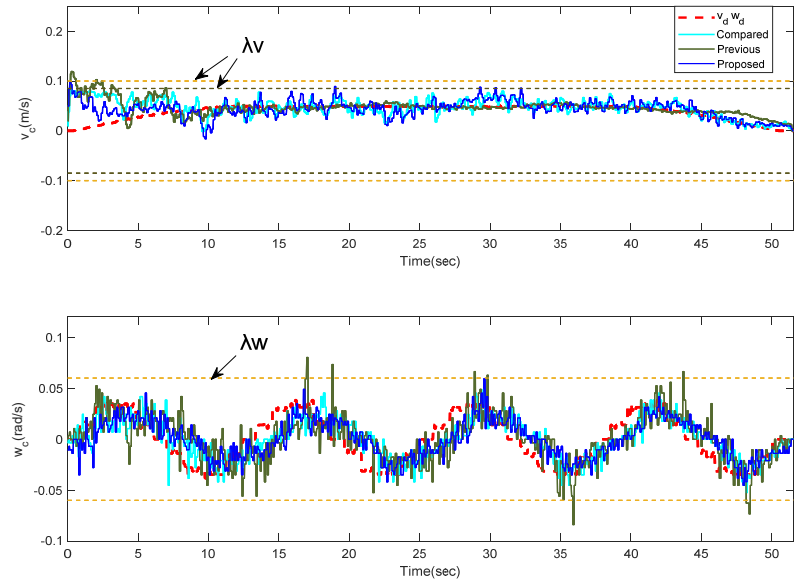


Figure 14. Velocities of the mobile robot. The yellow dotted lines denote the velocity saturation limits. The dark blue and light blue solid lines denote the method proposed in this work, respectively, and the green line corresponds to the previous method in [40].

Moreover, Table 1 presents a quantitative comparison between the proposed controller and the method described in [40], using the root mean square (RMS) errors for both position tracking ($\|x_h - x_{hd}\|_2$) and angular tracking ($\|\theta_c - \theta_d\|_2$). The results indicate that the proposed controller achieves lower RMS errors in both metrics compared to the method in [40]. For position tracking, the RMS error of the proposed method is slightly lower than the compared controller's error and significantly smaller than the error achieved with the method in [40]. Similarly, for angular tracking, the proposed controller exhibits a promising RMS error value, outperforming the compared controller and yielding a substantial improvement over the method in [40]. These results highlight the superior tracking accuracy of the proposed controller, demonstrating its effectiveness in reducing tracking errors and achieving better performance under the same experimental conditions. Figure 13

demonstrates the evolution of the tracking errors. In e_1, the proposed method gradually converges to zero over time while maintaining relatively small oscillations throughout the tracking process, demonstrating strong stability and disturbance rejection capabilities. In contrast, the method from [40] exhibits larger fluctuations over the entire time period and has a slower convergence rate. Regarding e_2, the error magnitude of the proposed method remains within a small range and gradually approaches zero as the experiment progresses. In contrast, the method from [40] shows significant oscillations in the corresponding error. For e_3, the proposed method exhibits some oscillations in the initial phase, but the amplitude gradually decreases. In comparison, the method from [40] exhibits persistent periodic oscillations with larger amplitudes throughout the entire process.

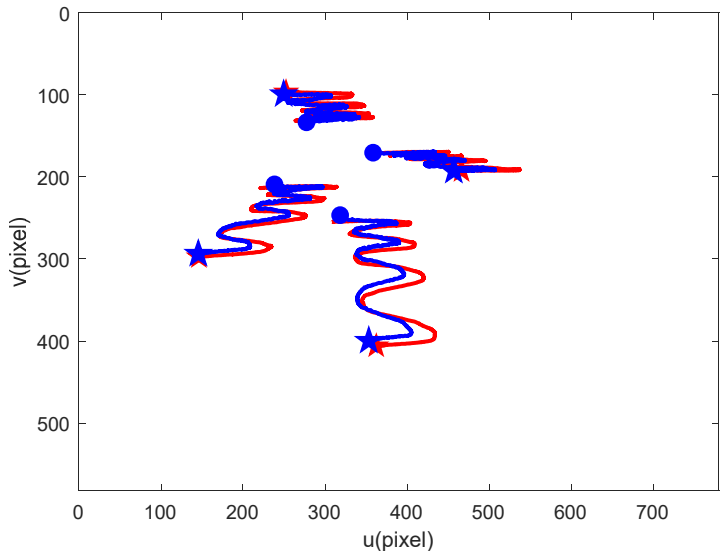


Figure 15. Image trajectories of feature points.

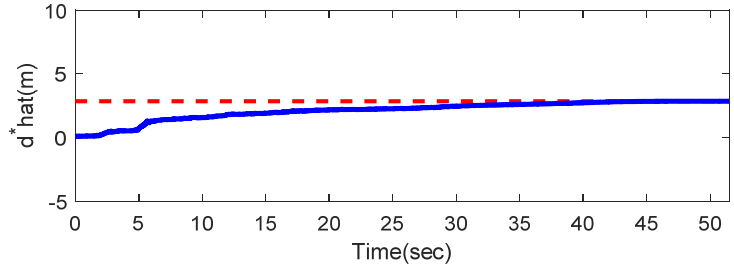


Figure 16. Evolution of the scene depth (dashed line: truth value of d^*).

Table 1. A comparison among the proposed controller, the compared controller, and [40].

RMS \ Controller	Proposed	Compared	[40]
$\|\mathrm{x}_h - x_{hd}\|_2$	0.0075695	0.0078967	0.011813
$\|\theta_\mathrm{c} - \theta_d\|_2$	0.023494	0.020562	0.040205

The velocity signal for the mobile robot is illustrated in Figure 14. The yellow and green dashed lines indicate different virtual velocity saturation limits λ_v. From this figure, it can be seen that, among the two different virtual velocity saturation limits, the velocities used in the method proposed in this work are within the saturation range, whereas the linear velocity of the comparison method exceeds the saturation limit in the range of 0.45–0.95 s. At the same time, the lower figure demonstrates that the angular velocity of the

method presented herein occurs within a specified limit. Therefore, this method can satisfy the constraints during the visual servo process.

Figure 15 presents the feature point trajectories obtained during the experiment. The red dashed lines represent the desired paths of the feature points, while the solid blue lines indicate the actual paths followed by the system. It can be seen that the actual feature trajectories closely follow the desired ones, demonstrating the method's effectiveness in achieving accurate trajectory tracking. This figure provides a visual comparison between the desired and actual feature movements in the image plane, highlighting the system's tracking performance. Furthermore, Figure 16 illustrates the evolution of the depth information. It can be observed that the estimated depth gradually converges to the true value as the experiment progresses. This figure demonstrates the effectiveness of the proposed depth estimation approach in achieving accurate and stable depth recognition. However, the estimation of the unknown depth in [40] is only intended to promote the tracking error to zero, while the actual value cannot be accurately estimated.

6. Conclusions

A novel monocular visual servoing scheme that satisfies velocity saturation constraints was successfully developed for wheeled mobile robots. The wheeled mobile robot was required to follow a desired time-varying trajectory derived from a prerecorded image while concurrently estimating the unknown depth. A homography-based algorithm was employed to estimate the robot's relative position within the scale space, followed by the construction of a visual tracking error model. An adaptive controller with velocity saturation limits was designed to address the tracking problems of the mobile robot and enable the velocity commands to remain within the allowed limits. In addition, an adaptive updating law was designed to estimate the unknown scene depth. Subsequently, the stability of the scheme was demonstrated by employing the Lyapunov technique, and the parameter boundedness was analyzed. Finally, a simulation and comparative experiment were performed to verify the effectiveness of the proposed method. Future research will focus on developing energy-efficient trajectory tracking methods to optimize energy consumption while ensuring system stability and tracking accuracy for improved operational efficiency and sustainability. In addition, we will explore the adaptability of our methods in complex 3D environments and investigate more advanced methods, such as applying techniques such as deep learning or multi-camera systems, to improve the tracking accuracy, depth estimation, and stability.

Author Contributions: Conceptualization, Q.Z.; methodology, Q.Z.; software, Q.Z. and F.S.; validation, Q.Z. and B.L.; formal analysis, Q.Z.; investigation, Q.Z.; resources, Q.Z. and B.L.; data curation, Q.Z.; writing—original draft preparation, Q.Z.; writing—review and editing, Q.Z. and B.L.; visualization, Q.Z.; supervision, B.L.; project administration, Q.Z. and B.L.; funding acquisition, B.L. All authors have read and agreed to the published version of the manuscript.

Funding: This research was funded in part by the National Natural Science Foundation of China under grants 61973234 and 62203326, and in part by the Tianjin Natural Science Foundation under grant 20JCYBJC00180.

Institutional Review Board Statement: Not applicable.

Informed Consent Statement: Not applicable.

Data Availability Statement: The source code presented in this study is available upon request from the corresponding author.

Acknowledgments: The authors would like to thank Tiangong University for the technical support and all members of our team for their contributions to the mobile robot experiments. The authors acknowledge the anonymous reviewers for their helpful comments on the manuscript.

Conflicts of Interest: The authors declare no conflicts of interest.

References

1. Chen, J.; Kim, W.-J. A human-following mobile robot providing natural and universal interfaces for control with wireless electronic devices. *IEEE/ASME Trans. Mechatron.* **2019**, *24*, 2377–2385. [CrossRef]
2. Cui, Z.; Li, W.; Zhang, X.; Chiu, P.W.Y.; Li, Z. Accelerated dual neural network controller for visual servoing of flexible endoscopic robot with tracking error, joint motion, and RCM constraints. *IEEE Trans. Ind. Electron.* **2021**, *69*, 9246–9257. [CrossRef]
3. Cui, Z.; Tang, X.; Hou, S.; Sun, H. Research on controllable stiffness of redundant cable-driven parallel robots. *IEEE/ASME Trans. Mechatron.* **2018**, *23*, 2390–2401. [CrossRef]
4. Li, Y.; Ding, L.; Zheng, Z.; Yang, Q.; Zhao, X.; Liu, G. A multi-mode real-time terrain parameter estimation method for wheeled motion control of mobile robots. *Mech. Syst. Signal Process.* **2018**, *104*, 758–775. [CrossRef]
5. Brown, J.; Sukkarieh, S. Design and evaluation of a modular robotic plum harvesting system utilizing soft components. *J. Field Robot.* **2021**, *38*, 289–306. [CrossRef]
6. Zhang, X.; Wang, R.; Fang, Y.; Li, B.; Ma, B. Acceleration-level pseudo-dynamic visual servoing of mobile robots with backstepping and dynamic surface control. *IEEE Trans. Syst. Man Cybern. Syst.* **2017**, *49*, 2071–2081. [CrossRef]
7. Cui, Z.; Huang, Y.; Li, W.; Chiu, P.W.Y.; Li, Z. Noise-resistant adaptive gain recurrent neural network for visual tracking of redundant flexible endoscope robot with time-varying state variable constraints. *IEEE Trans. Ind. Electron.* **2023**, *71*, 2694–2704. [CrossRef]
8. Li, Z.; Lai, B.; Wang, H.; Pan, Y. Homography-based visual servoing of robot pose under an uncalibrated eye-to-hand camera. *IEEE/ASME Trans. Mechatron.* **2023**, *29*, 1891–1902. [CrossRef]
9. Li, B.; Fang, Y.; Hu, G.; Zhang, X. Model-free unified tracking and regulation visual servoing of wheeled mobile robots. *IEEE Trans. Control Syst. Technol.* **2015**, *24*, 1328–1339. [CrossRef]
10. Qiu, Y.; Li, B.; Shi, W.; Zhang, X. Visual servo tracking of wheeled mobile robots with unknown extrinsic parameters. *IEEE Trans. Ind. Electron.* **2019**, *66*, 8600–8609. [CrossRef]
11. Xu, S.; Ou, Y.; Duan, J.; Wu, X.; Feng, W.; Liu, M. Robot trajectory tracking control using learning from demonstration method. *Neurocomputing* **2019**, *338*, 249–261. [CrossRef]
12. Shao, Z.; Zhang, J. Vision-based adaptive trajectory tracking control of wheeled mobile robot with unknown translational external parameters. *IEEE/ASME Trans. Mechatron.* **2023**, *29*, 358–365. [CrossRef]
13. Li, B.; Zhang, X.; Fang, Y.; Shi, W. Visual servoing of wheeled mobile robots without desired images. *IEEE Trans. Cybern.* **2018**, *49*, 2835–2844. [CrossRef] [PubMed]
14. Morrison, D.; Corke, P.; Leitner, J. Learning robust, real-time, reactive robotic grasping. *Int. J. Robot. Res.* **2020**, *39*, 183–201. [CrossRef]
15. Zinchenko, K.; Wu, C.-Y.; Song, K.-T. A study on speech recognition control for a surgical robot. *IEEE Trans. Ind. Inform.* **2016**, *13*, 607–615. [CrossRef]
16. Zhang, Z.; Zhang, L.; Deng, J.; Wang, M.; Wang, Z.; Cao, D. An enabling trajectory planning scheme for lane change collision avoidance on highways. *IEEE Trans. Intell. Veh.* **2021**, *8*, 147–158. [CrossRef]
17. Sun, Y.; Peng, Z.; Hu, J.; Ghosh, B.K. Event-triggered critic learning impedance control of lower limb exoskeleton robots in interactive environments. *Neurocomputing* **2024**, *564*, 126963. [CrossRef]
18. Wang, Y.; Sun, R.; Cheng, Q.; Ochieng, W.Y. Measurement quality control aided multi-sensor system for improved vehicle navigation in urban areas. *IEEE Trans. Ind. Electron.* **2023**, *71*, 6407–6417. [CrossRef]
19. Wang, H.; Guo, D.; Liang, X.; Chen, W.; Hu, G.; Leang, K.K. Adaptive vision-based leader–follower formation control of mobile robots. *IEEE Trans. Ind. Electron.* **2016**, *64*, 2893–2902. [CrossRef]
20. Shi, H.; Sun, G.; Wang, Y.; Hwang, K.-S. Adaptive image-based visual servoing with temporary loss of the visual signal. *IEEE Trans. Ind. Inform.* **2018**, *15*, 1956–1965. [CrossRef]
21. Lai, N.; Chen, Y.; Liang, J.; He, B.; Zhong, H.; Zhang, H.; Wang, Y. Image dynamics-based visual servo control for unmanned aerial manipulatorl with a virtual camera. *IEEE/ASME Trans. Mechatron.* **2022**, *27*, 5264–5274. [CrossRef]
22. Liang, X.; Liu, Y.-H.; Wang, H.; Chen, W.; Xing, K.; Liu, T. Leader-following formation tracking control of mobile robots without direct position measurements. *IEEE Trans. Autom. Control* **2016**, *61*, 4131–4137.
23. Yan, F.; Li, B.; Shi, W.; Wang, D. Hybrid visual servo trajectory tracking of wheeled mobile robots. *IEEE Access* **2018**, *6*, 24291–24298. [CrossRef]

24. Chen, Z.; Liu, Y.; He, W.; Qiao, H.; Ji, H. Adaptive-neural-network-based trajectory tracking control for a nonholonomic wheeled mobile robot with velocity constraints. *IEEE Trans. Ind. Electron.* **2020**, *68*, 5057–5067. [CrossRef]
25. Yu, J.; Shi, P.; Lin, C.; Yu, H. Adaptive neural command filtering control for nonlinear MIMO systems with saturation input and unknown control direction. *IEEE Trans. Cybern.* **2019**, *50*, 2536–2545. [CrossRef] [PubMed]
26. Zheng, Z.; Feroskhan, M. Path following of a surface vessel with prescribed performance in the presence of input saturation and external disturbances. *IEEE/ASME Trans. Mechatron.* **2017**, *22*, 2564–2575. [CrossRef]
27. Zhang, L.; Ma, C.; Liu, J. Enhancing four-axis machining center accuracy through interactive fusion of spatiotemporal graph convolutional networks and an error-controlled digital twin system. *J. Manuf. Process.* **2024**, *112*, 14–31. [CrossRef]
28. Wang, R.; Zhang, X.; Fang, Y.; Li, B. Visual servoing of mobile robots with input saturation at kinematic level. In Proceedings of the Image and Graphics: 9th International Conference, ICIG 2017, Shanghai, China, 13–15 September 2017.
29. Jiang, Z.-P.; Lefeber, E.; Nijmeijer, H. Saturated stabilization and tracking of a nonholonomic mobile robot. *Syst. Control Lett.* **2001**, *42*, 327–332.
30. Wang, R.; Zhang, X.; Fang, Y. Visual tracking of mobile robots with both velocity and acceleration saturation constraints. *Mech. Syst. Signal Process.* **2021**, *150*, 107274. [CrossRef]
31. Yin, Y.; Wang, Z.; Zheng, L.; Su, Q.; Guo, Y. Autonomous UAV navigation with adaptive control based on deep reinforcement learning. *Electronics* **2024**, *13*, 2432. [CrossRef]
32. Jiangdagger, Z.-P.; Nijmeijer, H. Tracking control of mobile robots: A case study in backstepping. *Automatica* **1997**, *33*, 1393–1399. [CrossRef]
33. Zhu, C. Intelligent robot path planning and navigation based on reinforcement learning and adaptive control. *J. Logist. Inform. Serv. Sci.* **2023**, *10*, 235–248.
34. Zhao, D.; Shao, D.; Cui, L. CTNet: A data-driven time-frequency technique for wind turbines fault diagnosis under time-varying speeds. *ISA Trans.* **2024**, *154*, 335–351. [CrossRef] [PubMed]
35. Parikh, A.; Kamalapurkar, R.; Chen, H.-Y.; Dixon, W.E. Homography based visual servo control with scene reconstruction. In Proceedings of the 2015 54th IEEE Conference on Decision and Control (CDC), Osaka, Japan, 15–18 December 2015.
36. Li, B.; Zhang, X.; Fang, Y.; Shi, W. Visual servo regulation of wheeled mobile robots with simultaneous depth identification. *IEEE Trans. Ind. Electron.* **2017**, *65*, 460–469. [CrossRef]
37. Zhang, K.; Chen, J.; Li, Y.; Zhang, X. Visual tracking and depth estimation of mobile robots without desired velocity information. *IEEE Trans. Cybern.* **2018**, *50*, 361–373. [CrossRef] [PubMed]
38. Liu, A.; Lai, G.; Xiao, H.; Liu, Z.; Zhang, Y.; Chen, C.P. Resilient adaptive trajectory tracking control for uncalibrated visual servoing systems with unknown actuator failures. *J. Franklin Inst.* **2024**, *361*, 526–542. [CrossRef]
39. Jo, K.; Chwa, D. Immersion-and-Invariance Fuzzy Adaptive Image-Based Visual Servoing of Omnidirectional Mobile Robots Considering Uncertain Feature Point Dynamics. *IEEE Trans. Intell. Veh.* **2024**, 1–14. [CrossRef]
40. Chen, J.; Dixon, W.E.; Dawson, M.; McIntyre, M. Homography-based visual servo tracking control of a wheeled mobile robot. *IEEE Trans. Robot.* **2006**, *22*, 406–416. [CrossRef]

Disclaimer/Publisher's Note: The statements, opinions and data contained in all publications are solely those of the individual author(s) and contributor(s) and not of MDPI and/or the editor(s). MDPI and/or the editor(s) disclaim responsibility for any injury to people or property resulting from any ideas, methods, instructions or products referred to in the content.